Astronomy & Astrophysics manuscript no. rrwelf_arxiv
December 6, 2016
©ESO 2016

arXiv:1612.01017v1 [astro-ph.HE] 3 Dec 2016

The electron energy-loss rate due to radiative recombination

Junjie Mao[1, 2], Jelle Kaastra[1, 2] and N. R. Badnell[3]

[1] SRON Netherlands Institute for Space Research, Sorbonnelaan 2, 3584 CA Utrecht, the Netherlands
[2] Leiden Observatory, Leiden University, Niels Bohrweg 2, 2300 RA Leiden, the Netherlands
[3] Department of Physics, University of Strathclyde, Glasgow G4 0NG, UK

Received date / Accepted date

ABSTRACT

Context. For photoionized plasmas, electron energy-loss rates due to radiative recombination (RR) are required for thermal equilibrium calculations, which assume a local balance between the energy gain and loss. While many calculations of total and/or partial RR rates are available from literature, specific calculations of associated RR electron energy-loss rates are lacking.
Aims. Here we focus on electron energy-loss rates due to radiative recombination of H-like to Ne-like ions for all the elements up to and including zinc ($Z = 30$), over a wide temperature range.
Methods. We use the AUTOSTRUCTURE code to calculate the level-resolved photoionization cross section and modify the ADASRR code so that we can simultaneously obtain level-resolved RR rate coefficients and associated RR electron energy-loss rate coefficients. The total RR rates and electron energy-loss rates of H I and He I are compared with those found in literature. Furthermore, we utilize and parameterize the weighted electron energy-loss factors (dimensionless) to characterize total electron energy-loss rates due to RR.
Results. The RR electron energy-loss data are archived according to the Atomic Data and Analysis Structure (ADAS) data class *adf48*. The RR electron energy-loss data are also incorporated into the SPEX code for detailed modelling of photoionized plamsas.

Key words. atomic data – atomic processes

1. Introduction

Astrophysical plasmas observed in the X-ray band can roughly be divided into two subclasses: collisional ionized plasmas and photoionized plasmas. Typical collisional ionized plasmas include stellar coronae (in coronal/collisional ionization equilibrium), supernova remnants (SNRs, in non-equilibrium ionization) and the intracluster medium (ICM). In a low-density, high-temperature collisional ionized plasma, e.g. ICM, collisional processes play an important role (for a review, see e.g. Kaastra et al. 2008). In contrast, in a photoionized plasma, photoionization, recombination and fluorescence processes are also important in addition to collisional processes. Both the equations for the ionization balance (also required for a collisional ionized plasma) and the equations of the thermal equilibrium are used to determine the temperature of the photoionized plasma. Typical photoionized plasmas in the X-ray band can be found in X-ray binaries (XRBs) and active galactic nuclei (AGN).

For collisional ionized plasmas, various calculations of total radiative cooling rates are available in the literature, such as Cox & Daltabuit (1971), Raymond et al. (1976), Sutherland & Dopita (1993), Schure et al. (2009), Foster et al. (2012) and Lykins et al. (2013). These calculations take advantage of full plasma codes like SPEX (Kaastra et al. 1996) and APEC (Smith et al. 2001), and do not treat individual energy-loss (cooling) processes separately. Total radiative cooling rates include the energy-loss of both the line emission and the continuum emission. The latter includes the energy-loss due to radiative recombination (RR). Even more specifically, the energy-loss due to RR can be separated into the electron energy-loss and the ion energy-loss.

Send offprint requests to: J. Mao, e-mail: J.Mao@sron.nl

On the other hand, for photoionized plasmas, the electron energy-loss rate due to RR is one of the fundamental parameters for thermal equilibrium calculations, which assume a local balance between the energy gain and loss. Energy can be gained via photoionization, Auger effect, Compton scattering, collisional ionization, collisional de-excitation and so forth. Energy-loss can be due to radiative recombination, dielectronic recombination, three body recombination, inverse Compton scattering, collisional excitation, bremsstrahlung, etc., as well as the line/continuum emission following these atomic processes. In fact, the energy-loss/gain of all these individual processes need to be known. The calculations of electron energy-loss rates due to RR in the Cloudy code (Ferland et al. 1998, 2013) are based on hydrogenic results (Ferland et al. 1992; LaMothe & Ferland 2001). In this manuscript, we focus on improved calculations of the electron energy-loss due to radiative recombination, especially providing results for He-like to Ne-like isoelectronic sequences.

While several calculations of RR rates, including the total rates and/or detailed rate coefficients, for different isoelectronic sequences are available, e.g. Gu (2003) and Badnell (2006), specific calculations of the associated electron energy-loss rate due to RR are limited. The pioneering work was done by Seaton (1959) for hydrogenic ions using the asymptotic expansion of the Gaunt factor for photoionization cross sections (PICSs).

By using a modified semi-classical Kramers formula for radiative recombination cross sections (RRCSs), Kim & Pratt (1983) calculated the total RR electron energy-loss rate for a few ions in a relatively narrow temperature range.

Ferland et al. (1992) used the *nl*-resolved hydrogenic PICSs provided by Storey & Hummer (1991) to calculate both *n*-

resolved RR rates ($\alpha_i^{\rm RR}$) and electron energy-loss rates ($L_i^{\rm RR}$). Contributions up to and include $n = 1000$ are taken into account.

Using the same *nl*-resolved hydrogenic PICSs provided by Storey & Hummer (1991), Hummer (1994) calculated the RR electron energy-loss rates for hydrogenic ions in a wide temperature range. In addition, Hummer & Storey (1998) calculated PICSs of He I (photoionizing ion) for $n \leq 25$ with their close-coupling $\boldsymbol{R}$-matrix calculations. Together with hydrogenic (Storey & Hummer 1991) PICSs for $n > 25$ (up to $n = 800$ for low temperatures), the RR electronic energy-loss rate coefficient of He I (recombined ion) was obtained.

Later, LaMothe & Ferland (2001) used the exact PICSs from the Opacity Project (Seaton et al. 1992) for $n < 30$ and PICSs of Verner & Ferland (1996) for $n \geq 30$ to obtain *n*-resolved RR electron energy-loss rates for hydrogenic ions in a wide temperature range. The authors introduced the ratio of β/α (dimensionless), with $\beta = L/kT$ and L the RR electron energy-loss rate. The authors also pointed out that β/α changes merely by 1 dex in a wide temperature range meanwhile α and β change more than 12 dex.

In the past two decades, more detailed and accurate calculations of PICSs of many isoelectronic sequences have been carried out (e.g. Badnell 2006), which can be used to calculate specifically the electron energy-loss rates due to RR.

Currently, in the SPEX code (Kaastra et al. 1996), the assumption that the mean kinetic energy of a recombining electron is $3kT/4$ (Kallman & McCray 1982) is applied for calculating the electron energy-loss rate due to RR. Based on the level-resolved PICSs provided by the AUTOSTRUCTURE[1] code (v24.24.3, Badnell 1986), the electron energy-loss rates due to RR are calculated for the H-like to Ne-like isoelectronic sequences for elements up to and including Zn ($Z = 30$) in a wide temperature range. Subsequently, the electron energy-loss rate coefficients ($\beta = L/kT$) are weighted with respect to the total RR rates ($\alpha_{\rm t}$), yielding the weighted electron energy-loss factors ($f = \beta/\alpha_{\rm t}$, dimensionless). The weighted electron energy-loss factors can be used, together with the total RR rates, to update the description of the electron energy-loss due to RR in the SPEX code or other codes.

In Sect. 2, we describe the details of the numerical calculation from PICSs to the electron energy-loss rate due to RR. Typical results are shown graphically in Sect. 3. Parameterization of the weighted electron energy-loss factors is also illustrated in Sect. 3.1. The detailed RR electron energy-loss data are archived according to the Atomic Data and Analysis Structure (ADAS) data class *adf48*. Full tabulated (unparameterized and parameterized) weighted electron energy-loss factors are available in CDS. Comparison of the results for H I and He I can be found in Section 4.1. The scaling of the weighted electron energy-loss factors with respect to the square of the ionic charge of the recombined ion can be found in Section 4.2. We also discuss the electron and ion energy-loss due to RR (Section 4.3) and the total RR rates (Section 4.4).

Throughout this paper, we refer to the recombined ion when we speak of the radiative recombination of a certain ion, since the line emission following the radiative recombination comes from the recombined ion. Furthermore, only RR from the ground level of the recombining ion is discussed here.

[1] http://amdpp.phys.strath.ac.uk/autos/

2. Methods

2.1. Cross sections

The AUTOSTRUCTURE code is used for calculating level-resolved non-resonant PICSs under the intermediate coupling ("IC") scheme (Badnell & Seaton 2003). The atomic and numerical details can be found in Badnell (2006), we briefly state the main points here. We use the Slater-Type-Orbital model potential to determine the radial functions. PICSs are calculated first at zero kinetic energy of the escaping electron, and subsequently on a z-scaled logarithmic energy grid with three points per decade, ranging from $\sim z^2 10^{-6}$ to $z^2 10^2$ ryd, where z is the ionic charge of the photoionizing ion/atom. PICSs at even higher energies are at least several orders of magnitude smaller compared to PICSs at zero kinetic energy of the escaping electron. Nonetheless, it still can be important, especially for the *s*- and *p*-orbit, to derive the RR data at the high temperature end. We take advantage of the analytical hydrogenic PICSs (calculated via the dipole radial integral, Burgess 1965) and scale them to the PICS with the highest energy calculated by AUTOSTRUCTURE to obtain PICSs at very high energies. Note that fully *nLS J*-resolved PICSs for those levels with $n \leq 15$ and $l \leq 3$ are calculated specifically. For the rest of the levels, we use the fast, accurate and recurrence hydrogenic approximation (Burgess 1965). Meanwhile, bundled-*n* PICSs for $n = 16$, 20, 25, 35, 45, 55, 70, 100, 140, 200, 300, 450, 700, 999 are also calculated specifically in order to derive the total RR and electron energy-loss rates (interpolation and quadrature required as well).

The inverse process of dielectronic and radiative recombination is resonant and non-resonant photoionization, respectively. Therefore, radiative recombination cross sections (RRCSs) are obtained through the Milne relation under the principle of detailed balance (or microscopic reversibility) from non-resonant PICSs.

2.2. Rate coefficients

The RR rate coefficient is obtained by

$$\alpha_i(T) = \int_0^\infty v\, \sigma_i(v)\, f(v,\, T)\, dv\,, \tag{1}$$

where v is the velocity of the recombining electron, σ_i is the individual detailed (level/term/shell-resolved) RRCS, $f(v,\, T)$ is the probability density distribution of the velocity of the recombining electrons for the electron temperature T. The Maxwell-Boltzmann distribution for the free electrons is adopted throughout the calculation, with the same quadrature approach as described in Badnell (2006). Accordingly, the total RR rate per ion/atom is

$$\alpha_{\rm t}(T) = \sum_i \alpha_i(T)\,. \tag{2}$$

Total RR rates for all the isoelectronic sequences, taking contributions up to $n = 10^3$ into account (see its necessity in Section 3).

The RR electron energy-loss rate coefficient is defined as (e.g. Osterbrock 1989)

$$\beta_i(T) = \frac{1}{kT} \int_0^\infty \frac{1}{2}\, m\, v^3\, \sigma_i(v)\, f(v,\, T)\, dv\,, \tag{3}$$

The total electron energy-loss rate due to RR is obtained simply by adding all the contributions from individual captures,

$$L_{\rm t}(T) = \sum_i L_i = kT \sum_i \beta_i\,, \tag{4}$$

which can be identically derived via

$$L_{\rm t}(T) = kT\ \alpha_{\rm t}(T)\ f_{\rm t}(T)\ , \tag{5}$$

where

$$f_{\rm t}(T) = \frac{\sum_i\ \beta_i(T)}{\alpha_{\rm t}(T)}\ , \tag{6}$$

is defined as the weighted electron energy-loss factor (dimensionless) hereafter.

The above calculation of the electron energy-loss rates is realized by adding Equation (3) into the archival post-processor FORTRAN code ADASRR[2] (v1.11). Both the level-resolved and bundled-n/nl RR data and the RR electron energy-loss data are obtained. The output files have the same format of *adf48* with RR rates and electron energy-loss rates in the units of cm^3 s^{-1} and ryd cm^3 s^{-1}, respectively. Note that ionization potentials of the ground level of the recombined ions from NIST[3] (v5.3) are adopted to correct the conversion from PICSs to RRCSs at low kinetic energy for low-charge ions. We should point out that although the level-resolved and bundled-nl/n RR data are, in fact, available on OPEN ADAS[4], given the fact that we use the latest version of the AUTOSTRUCTURE code and a modified version of the ADASRR code, here we re-calculate the RR data, which are used together with the RR electron energy-loss data to derive the weighted electron energy-loss factor $f_{\rm t}$ for consistency. In general, our re-calculate RR data are almost identical to those on OPEN ADAS, except for a few many-electron ions at the the high temperature end, where our re-calculated data differ by a few percent. Whereas, both RR data and electron energy-loss data are a few orders of magnitude smaller compared to those at the lower temperature end, thus, the above mentioned difference has negligible impact on the accuracy of the weighted electron energy-loss factor (see also in Section 4.4).

For all the isoelectronic sequences discussed here, the conventional ADAS 19-point temperature grid $z^2(10 - 10^7)$ K is used.

3. Results

For each individual capture due to radiative recombination, when $kT \ll I$, where I is the ionization potential, the RR electron energy-loss rate L_i is nearly identical to $kT\ \alpha_i$, since the Maxwellian distribution drops exponentially for $E_{\rm k} \gtrsim kT$, where $E_{\rm k}$ is the kinetic energy of the free electron before recombination. On the other hand, when $kT \gg I$, the RR electron energy-loss rate is negligible compared with $kT\ \alpha_i$. As in an electron-ion collision, when the total energy in the incident channel nearly equals that of a closed-channel discrete state, the channel interaction may cause the incident electron to be captured in this state (Fano & Cooper 1968). That is to say, those electrons with $E_{\rm k} \simeq I$ are preferred to be captured, thus, $L_i \sim I\ \alpha_i$. Figure 1 shows the ratio of $\beta_i/\alpha_i = L_i/(kT\alpha_i)$ for representative $nLS\,J$-resolved levels (with $n \leq 8$) of He-like Mg XI .

In terms of capturing free electrons into individual shells (bundled-n), due to the rapid decline of the ionization potentials for those very high-n shells, the ionization potentials can be comparable to kT, if not significantly less than kT, at the low temperature end. Therefore we see the significant difference between the top panel (low-n shells) and middle panel (high-n shells) of

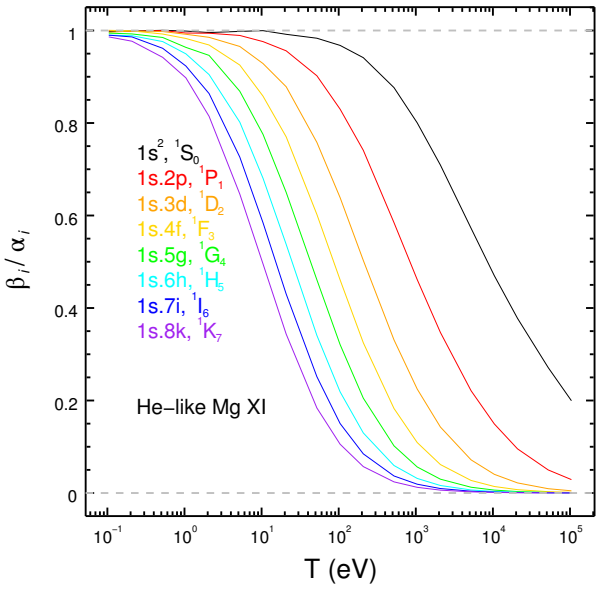

Fig. 1. For He-like Mg XI, the ratio between level-resolved electron energy-loss rates L_i and the corresponding radiative recombination rates times the temperature of the plasma, i.e. β_i/α_i (not be confused with $\beta_i/\alpha_{\rm t}$), where i refers to the $nLS\,J$-resolved levels with $n \leq 8$ (shown selectively in the plot).

Figure 2. In order to achieve adequate accuracy, contributions from high-n shells (up to $n \leq 10^3$) ought to be included. The middle panel of Figure 2 shows clearly that even for $n = 999$ (the line at the bottom), at the low temperature end, the ratio between $\beta_{n=999}$ and $\alpha_{n=999}$ does not drop to zero. Nevertheless, the bottom panel of Figure 2 illustrates the advantage of weighting the electron energy-loss rate coefficients with respect to the total RR rates, i.e. $\beta_i/\alpha_{\rm t}$, which approaches zero more quickly. At least, for the next few hundreds shells following $n = 999$, their weighted electron energy-loss factors should be no more than 10^{-5}, thus, their contribution to the total electron energy-loss rate should be less than 1%.

The bottom panels of Figure 3 and 4 illustrate the weighted electron energy-loss factors for He-like isoelectronic sequences (He, Si and Fe) and Fe isonuclear sequence (H-, He-, Be- and N-like), respectively. The deviation from (slightly below) unity at the lower temperature end is simply due to the fact that the weighted electron energy-loss factors of the very high-n shells are no longer close to unity (Figure 2, middle panel). The deviation from (slightly above) zero at the high temperature end is because the ionization potentials of the first few low-n shells can still be comparable to kT, while sum of these n-resolved RR rates are more or less a few tens of percent of the total RR rates.

Due to the non-hydrogenic screening of the wave function for low-nl states in low-charge many-electron ions, the characteristic high-temperature bump is present in not only the RR rates (see Figure 4 in Badnell 2006, for an example) but also in the electron energy-loss rates. The feature is even enhanced in the weighted electron energy-loss factor.

[2] http://amdpp.phys.strath.ac.uk/autos/ver/misc/adasrr.f
[3] http://physics.nist.gov/PhysRefData/ASD/ionEnergy.html
[4] http://open.adas.ac.uk/adf48

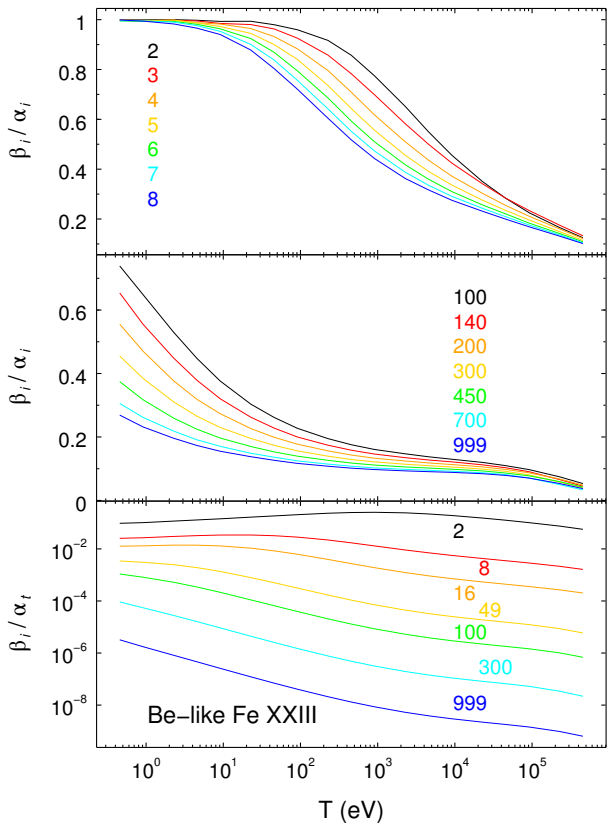

Fig. 2. Ratios of β_i/α_i for Be-like Fe XXIII (upper and middle panel) and ratios of β_i/α_t (bottom panel) where i refers to the shell number. Low- and high-n shell results are shown selectively in the plot. The upper panel shows all the shells with $n \leq 8$. The middle panel shows shells with n =100, 140, 200, 300, 450, 700 and 999. In the lower panel the shells are n = 2, 8, 16, 49, 100, 300, 999.

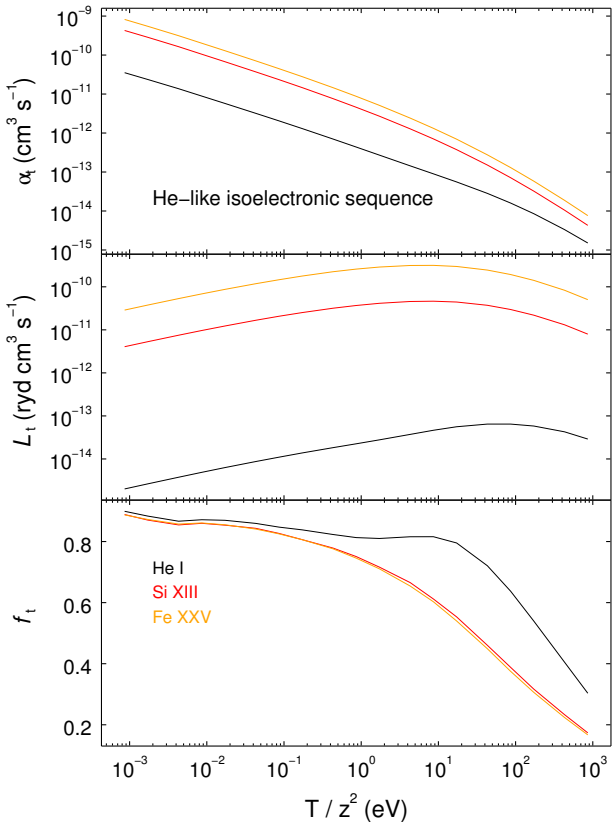

Fig. 3. The total RR rates α_t (top), electron energy-loss rates L_t (middle) and weighted electron energy-loss factors f_t (bottom) of He-like isoelectronic sequences for ions including He I (black), Si XIII (red) and Fe XXV (orange). The temperature is down-scaled by z^2, where z is the ionic charge of the recombined ion, to highlight the discrepancy between hydrogenic and non-hydrogenic. The captures to form the He I shows non-hydrogenic feature in the bottom panel.

3.1. Parameterization

We parameterize the ion/atom-resolved radiative recombination electron energy-loss factors using the same fitting strategy described in Mao & Kaastra (2016), with the model function of

$$f_t(T) = a_0\, T^{-b_0 - c_0 \log T} \left(\frac{1 + a_2 T^{-b2}}{1 + a_1 T^{-b1}}\right), \tag{7}$$

where the electron temperature T is in units of eV, a_0 and b_0 are primary fitting parameters, c_0, $a_{1,\,2}$ and $b_{1,\,2}$ are additional fitting parameters. The additional parameters are frozen to zero if they are not used. Furthermore, we constrain b_{0-2} to be within -10.0 to 10.0 and c_0 between 0.0 and 1.0. The initial values of the two primary fitting parameters a_0 and b_0 are set to unity together with the four additional fitting parameters $a_{1,\,2}$ and $b_{1,\,2}$ if they are thawn. Conversely, the initial value of c_0, if it is thawn, is set to either side of its boundary, i.e. $c_0 = 0.0$ or $c_0 = 1.0$ (both fits are performed).

In order to estimate the goodness of fit, the fits are performed with a set of artificial relative errors (r). We started with $r = 0.625\%$, following with increasing the artificial relative error by a factor of two, up to and including 2.5%. The chi-squared statistics adopted here are

$$\chi^2 = \sum_{i=1}^{N} \left(\frac{n_i - m_i}{r\, n_i}\right)^2, \tag{8}$$

where n_i is the ith numerical calculation result and m_i is the ith model prediction (Equation 7).

For the model selection, we first fit the data with the simplest model (i.e. all the five additional parameters are frozen to zero), following with fits with free additional parameters step by step. Thawing one additional parameter decreases the degrees of freedom by one, thus, only if the obtained statistics (χ^2) of the more complicated model improves by at least 2.71, 4.61, 6.26, 7.79 and 9.24 for one to five additional free parameter(s), respectively, the more complicated model is favored (at a 90% nominal confidence level).

Parameterizations of the ion/atom-resolved RR weighted electron energy-loss factors for individual ions/atoms in H-like to Ne-like isoelectronic sequences were performed. A typical fit for non-hydrogenic systems is shown in Figure 5 for N-like iron (Fe XX). The fitting parameters can be found in Table 2. Again, the weighted energy-loss factor per ion/atom is close to unity at

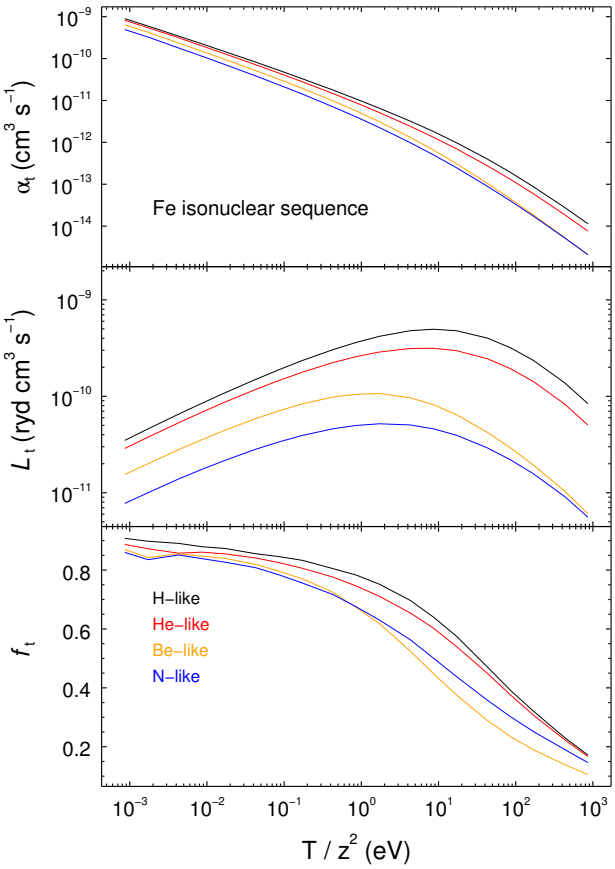

Fig. 4. Top panel is total RR rates α_t of the Fe isonuclear sequence, including H- (black), He- (red), Be- (orange) and N-like (blue); Middle panel is the RR electron energy-loss rates L_t; And bottom panel is the weighted electron energy-loss factors f_t. The temperature of the plasma is down-scaled by z^2, as in Figure 3.

low temperature end and drops towards zero rapidly at the high temperature end.

In Figure 6 we show the histogram of maximum deviation $\delta_{\max}$ (in percent) between the fitted model and the original calculation for all the ions considered here. In short, our fitting accuracy is within 4%, and even accurate ($\lesssim$ 2.5%) for the more important H-like, He-like and Ne-like isoelectronic sequences.

In addition, we also fit specifically the Case A ($f_A = \beta_t/\alpha_t$) and Case B (Baker & Menzel 1938, $f_B = \beta_{n\geq2}/\alpha_{n\geq2}$) RR weighted electron energy-loss factors of H I (Figure 7) and He I (Figure 8). Typical unparameterized factors (f_A and f_B) and fitting parameters can be found in Table 1 and 2, respectively.

4. Discussions

4.1. Comparison with previous results for H I and He I

Figure 9 shows a comparison of RR rates (α_t^{RR}), electron energy-loss rates (L_t^{RR}), weighted electron energy-loss factors (f_t^{RR}) from this work, Seaton (1959, blue), Ferland et al. (1992, orange) and Hummer (1994, red). Since both Ferland et al. (1992) and Hummer (1994) use the same PICSs (Storey & Hummer

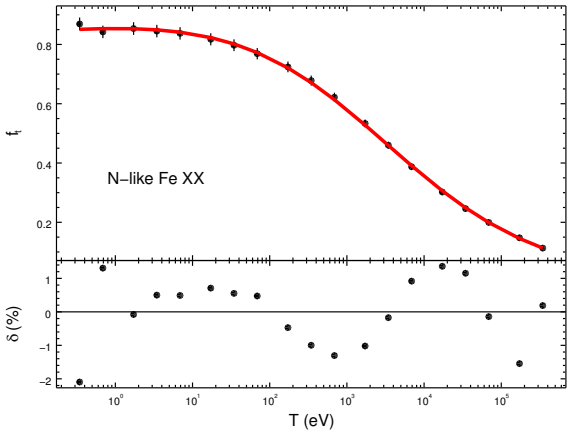

Fig. 5. The RR weighted electron energy-loss factor for N-like iron (Fe xx). The black dots in both panels (associated with artificial error bars of 2.5% in the upper one) are the calculated weighted electron energy-loss factor. The red solid line is the best-fit. The lower panel shows the deviation (in percent) between the best-fit and the original calculation.

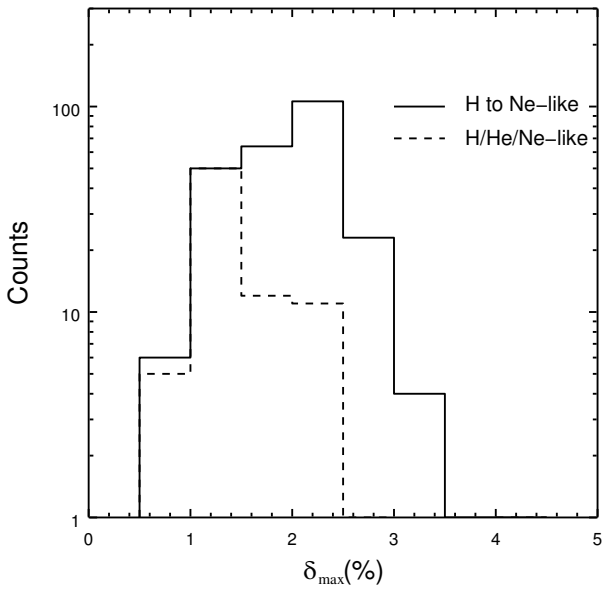

Fig. 6. The histogram of maximum deviation in percent ($\delta_{\max}$) for all the ions considered here, which reflects the overall goodness of our parameterization. The dashed-histogram is the statistics of the more important H-like, He-like and Ne-like isoelectronic sequences, while the solid one is the statistics of all the isoelectronic sequences.

1991), the two results are highly consistent as expected. The Case A and Case B results of this work are also consistent within 1% at the low temperature end, and increase to ~5% (underestimation). For the high temperature end ($T \gtrsim 0.1$ keV), since the ion fraction of H I is rather low (almost completely ionized), the present calculation is still acceptable. A similar issue towards to the high temperature end is also found in the Case A results of Seaton (1959), with a relatively significant overestimation ($\gtrsim$ 5%) from the other three calculations.

Table 2. Fitting parameters of RR weighted electron energy-loss factors for H I, He I and Fe xx. For the former two, both Case A and Case B results are included.

s	Z	Case	a_0	b_0	c_0	a_1	b_1	a_2	b_2	$\delta_{\max}$
1	1	A	8.655E+00	5.432E-01	0.000E+00	1.018E+01	5.342E-01	0.000E+00	0.000E+00	1.2%
1	1	B	2.560E+00	4.230E-01	0.000E+00	2.914E+00	4.191E-01	0.000E+00	0.000E+00	2.1%
2	2	A	2.354E+00	3.367E-01	0.000E+00	6.280E+01	8.875E-01	2.133E+01	5.675E-01	1.5%
2	2	B	1.011E+04	1.348E+00	4.330E-03	1.462E+04	1.285E+00	0.000E+00	0.000E+00	3.5%
7	26	A	2.466E+01	4.135E-01	0.000E+00	2.788E+01	4.286E-01	0.000E+00	0.000E+00	2.1%

Notes. s is the isoelectronic sequence number of the recombined ion, Z is the atomic number of the ion, a_{0-2}, b_{0-2} and c_0 are the fitting parameters and $\delta_{\max}$ is the maximum deviation (in percent) between the "best-fit" and original calculation. Case A and Case B refers to β_t/α_t and $\beta_{n\geq 2}/\alpha_{n\geq 2}$ RR weighted electron energy-loss factors, respectively. Machine readable fitting parameters and maximum deviation (in percent) for the total weighted electron energy loss factors for all the ions considered here are available on CDS.

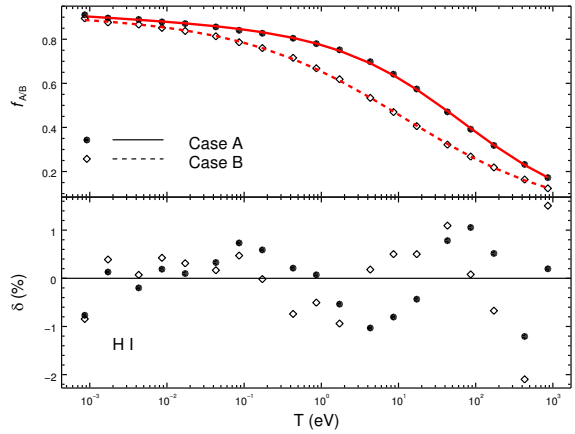

Fig. 7. The Case A (solid line, filled circles) and Case B (dashed line, empty diamonds) RR weighted electron energy-loss factor ($f_{A/B}$) for H I. The black dots in both panels (associated with artificial error bars in the upper one) are the calculated weighted electron energy-loss factor. The red solid line is the best-fit. The lower panel shows the deviation (in percent) between the best-fit and the original calculation.

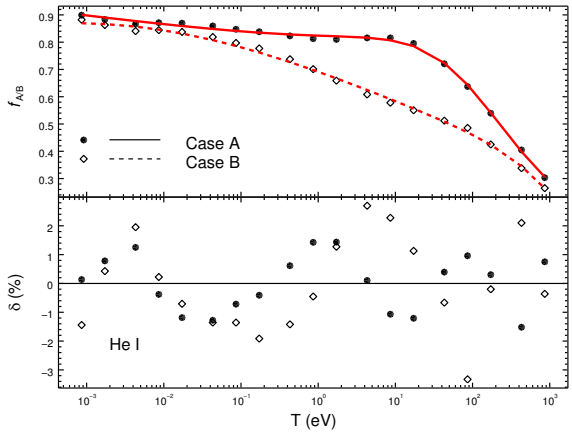

Fig. 8. Similar to Figure 7 but for He I.

Table 1. Unparameterize of RR weighted electron energy-loss factors for H I, He I and Fe xx. For the former two, both Case A and Case B results are treated seperately.

T/z^2 K	H I Case A	H I Case B	He I Case A	He I Case B	Fe xx Case A
10^1	0.911	0.895	0.899	0.882	0.869
10^2	0.879	0.851	0.871	0.844	0.845
10^3	0.841	0.786	0.847	0.797	0.797
10^4	0.780	0.668	0.813	0.701	0.678
10^5	0.642	0.470	0.816	0.578	0.460
10^6	0.392	0.268	0.637	0.486	0.246
10^7	0.172	0.123	0.303	0.265	0.113

Notes. Machine readable unparameterized Case A factors for all the ions considered here are available on CDS.

Likewise, the comparison for He I between this work and Hummer & Storey (1998) is presented in Figure 10. The Case A and Case B results from both calculations agree well (within 2%), at the low temperature end ($T \lesssim 2.0$ eV). At higher temperatures with $T \gtrsim 2$ eV, the RR rate and electron energy-loss rate for He I are not available in Hummer & Storey (1998).

4.2. Scaling with z^2

Previous studies of hydrogenic systems, Seaton (1959); Ferland et al. (1992); Hummer & Storey (1998), all use z^2 scaling for $\alpha_t^{\rm RR}$. That is to say, $\alpha_t^X = z^2\ \alpha_t^{\rm H}$, where z is the ionic charge of the recombined ion X. The same z^2 scaling also applies for $\beta_t^{\rm RR}$ (or $L_t^{\rm RR}$). LaMothe & Ferland (2001) also pointed out that the shell-resolved ratio of f_n^{RR} ($=\beta_n^{\rm RR}/\alpha_n^{\rm RR}$) can also be scaled with z^2/n^2, i.e. $f_n^X = \frac{z^2}{n^2}\ f_n^{\rm H}$ with n refers to the principle quantum number.

In the following, we merely focus on the scaling for the ion/atom-resolved data set. We show in the top panel of Figure 11 the ratios of f_t/z^2 for H-like ions. Apparently, from the bottom panel of Figure 11, the z^2 scaling for the H-like isoelectronic sequence is accurate within 2%. For the rest of the isoelectronic sequences, for instance, the He-like isoelectronic sequence shown in Figure 12, the z^2 scaling applies at the low temperature end, whereas, the accuracies are poorer toward the high temperature end. We also show the z^2 scaling for the Fe isonuclear sequence in Figure 13.

4.3. Radiative recombination continua

We restrict the discussion above for the RR energy-loss of the electrons in the plasma only. The ion energy-loss of the ions due to RR can be estimated as $P^{\rm RR} \sim I_i\ \alpha_i$, where I_i is the ionization potential of the level/term the free electron is captured into, and α_i is the corresponding RR rate coefficient. Whether to

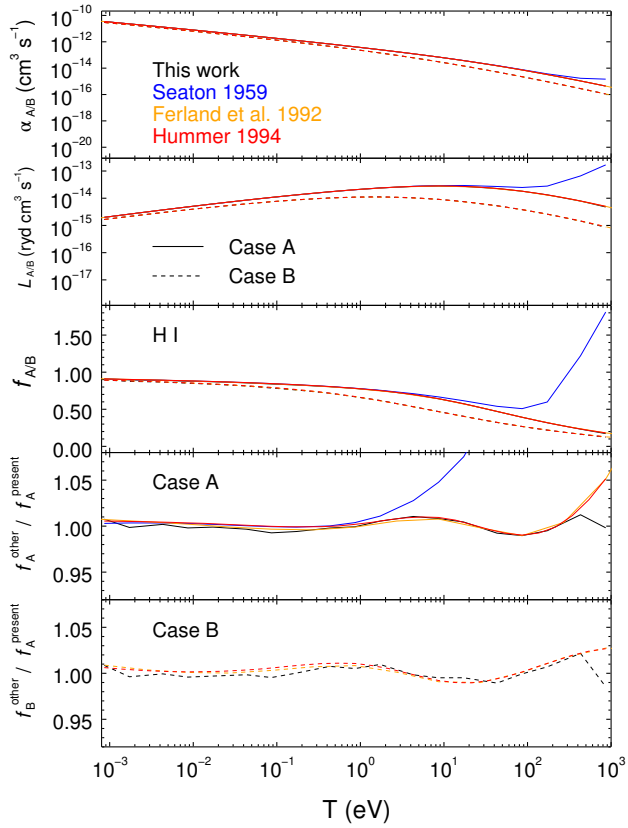

Fig. 9. The comparison of the RR data for H I among results from this work (black), Seaton (1959, blue), Ferland et al. (1992, orange) and Hummer (1994, red). Both results of case A (solid lines) and case B (dashed lines) are shown. The total RR rates ($\alpha^{\rm RR}_{\rm A/B}$) and electron energy-loss rates ($L^{\rm RR}_{\rm A/B}$) are shown in the top two panels. The RR weighted electron energy-loss factors ($f_{\rm A/B}$) are shown in the middle panel. The ratios of $f_{\rm A/B}$ from this work and previous works with respect to the fitting results (Equation 7 and Table 2) of this work, i.e. $f^{\rm other}_{\rm A/B}/f^{\rm present}_{\rm A/B}$, are shown in the bottom two panels.

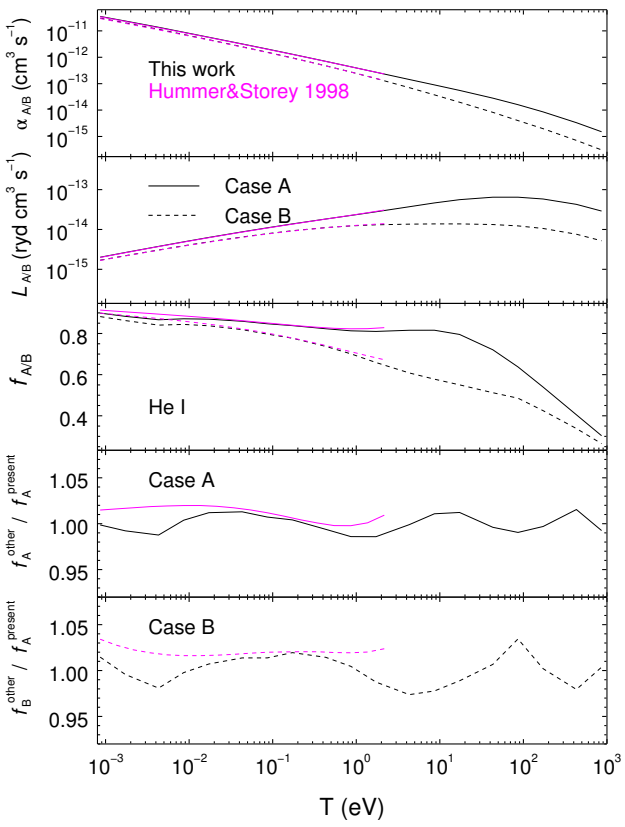

Fig. 10. Similar to Figure 10 but for He I between this work (black) and Hummer & Storey (magenta 1998). The latter one only provides data with $T \le 10^{4.4}$ K.

include the ionization potential energies as part of the total internal energy of the plasma is not critical, as long as the entire computation of the net energy gain/loss is self-consistent (see a discussion in Gnat & Ferland 2012). On the other hand, when interpreting the emergent spectrum due to RR, such as the radiative recombination continua (RRC) for a low-density plasma, the ion energy-loss of the ion is essentially required. The RRC emissivity (Tucker & Gould 1966) can be obtained via

$$\frac{dE^{\rm RRC}}{dt\,dV} = \int_0^\infty n_{\rm e}\,n_{\rm i}\left(I+\frac{1}{2}mv^2\right)v\,\sigma(v)\,f(v,\,kT)dv = n_{\rm e}\,n_{\rm i} I\,(1+f_{\rm t}\,kT/I)\,\alpha_{\rm t}\,, \quad (9)$$

where $n_{\rm e}$ and $n_{\rm i}$ are the electron and (recombining) ion number density, respectively. Generally speaking, the ion energy-loss of the ion dominates the electron energy-loss of the electrons, since $f_{\rm t}$ is of the order of unity while $kT \lesssim I$ holds for those X-ray photoionizing plasmas in XRBs (Liedahl & Paerels 1996), AGN (Kinkhabwala et al. 2002) and recombining plasmas in SNRs (Ozawa et al. 2009). Figure 14 shows the threshold temperature above which the electron energy-loss via RR cannot be neglected compared to the ion energy-loss. For hot plasmas with $kT \gtrsim 2$ keV, the electron energy-loss is comparable to the ion energy-loss for $Z > 5$. It is necessary to emphasize that we refer to the electron temperature T of the plasma here, which is not necessarily identical to the ion temperature of the plasma, in particular, in the nonequilibrium ionization scenario.

4.4. Total radiative recombination rate

Various calculations of (total or shell/term/level-resolved) RR data are available from the literature. Historically, different approaches have been used for calculating the total RR rates, including the Dirac-Hartree-Slater method (Verner et al. 1993) and the distorted-wave approximation (Gu 2003; Badnell 2006). Additionally, Nahar and coworkers (e.g. Nahar 1999) obtained the total (unified DR + RR) recombination rate for various ions with their ***R***-matrix calculations. Different approaches can lead to different total RR rates (see a discussion in Badnell 2006), as well as the Individual term/level-resolved RR rate coefficients, even among the most advanced ***R***-matrix calculations. Nevertheless, the bulk of the total RR rates for various ions agrees well among each other. As for the detailed RR rate coefficients, consequently, the detailed RR electron energy-loss rate, as long as the difference among different methods are within a few percent and given

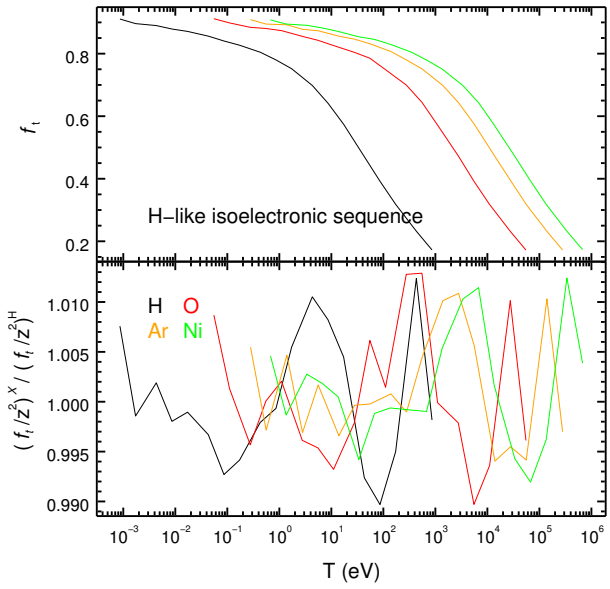

Fig. 11. The z^2 scaling for the H-like isoelectronic sequence (Case A), including H I (black), O VIII (red), Ar XVIII (orange) and Ni XXVIII (green). The top panel shows the ratios of f_t/z^2 as a function of electron temperature (T). The bottom panel is the ratio of $(f_t/z^2)^X$ for ion X with respect to the ratio of $(f_t/z^2)^{\rm H}$ for H.

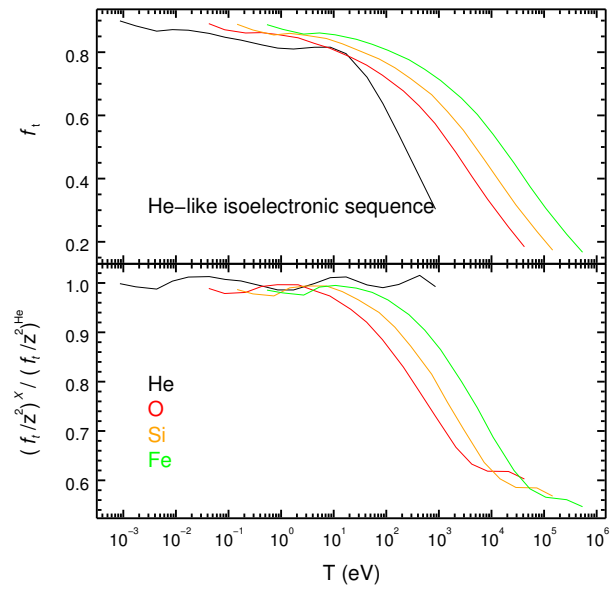

Fig. 12. Similar to Figure 11 but for the z^2 scaling for the He-like isoelectronic sequences.

the fact that each individual RR is $\lesssim 10\%$ of the total RR rate for a certain ion/atom, the final difference in the total weighted electron energy-loss factors f_t are still within 1%. In other words, although we used the re-calculated total RR rate (Section 2.2) to derive the weighted electron energy-loss factors, we assume these factors can still be applied to other total RR rates.

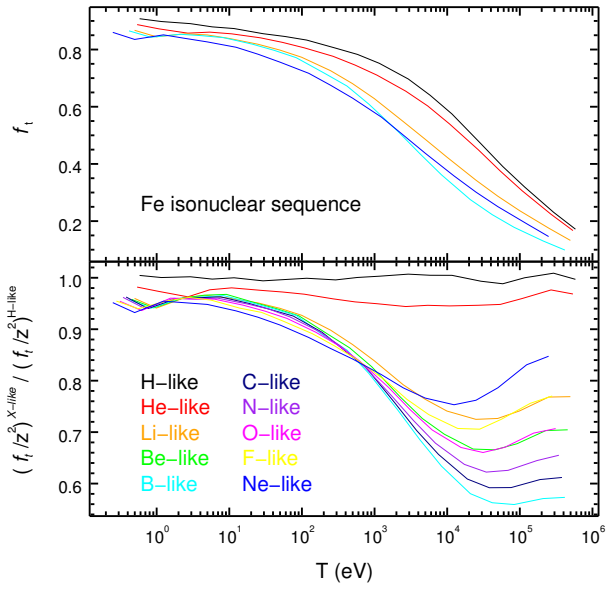

Fig. 13. The z^2 scaling for the Fe isonuclear sequence. The top panel shows the ratios of f_t/z^2 as a function of electron temperature (T). The bottom panel is the ratio of $(f_t/z^2)^{X-\rm like}$ for X-like Fe with respect to the ratio of $(f_t/z^2)^{\rm H-like}$ for H-like Fe XXVI.

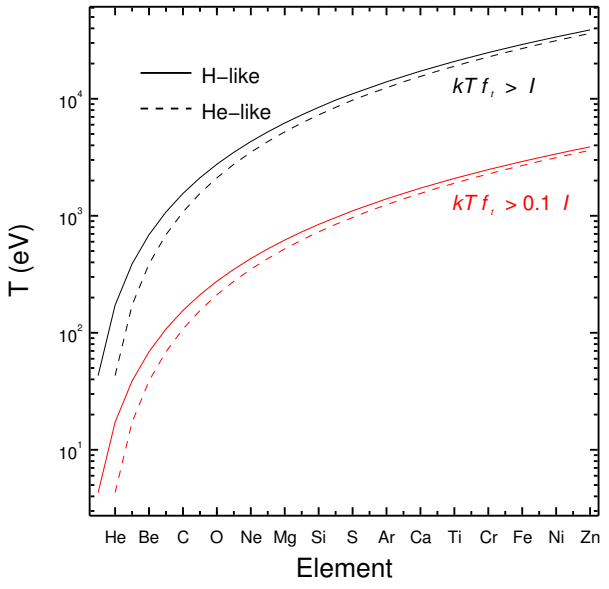

Fig. 14. The threshold temperature above which the electron energy-loss via RR cannot be neglected, compared to the ion energy-loss, for H-like (solid lines) and He-like ions (dashed lines).

Acknowledgements. J.M. acknowledges discussions and support from M. Mehdipour, A. Raassen, L. Gu and M. O'Mullane. We thank the referee, G. Ferland, for the valuable comments on the manuscript SRON is supported financially by NWO, the Netherlands Organization for Scientific Research.

References

Badnell, N. R. 1986, Journal of Physics B Atomic Molecular Physics, 19, 3827
Badnell, N. R., & Seaton, M. J. 2003, Journal of Physics B Atomic Molecular Physics, 36, 4367
Badnell, N. R. 2006, ApJS, 167, 334
Baker, J. G., & Menzel, D. H. 1938, ApJ, 88, 52
Burgess, A. 1965, MmRAS, 69, 1
Cox, D. P., & Daltabuit, E. 1971, ApJ, 167, 113
Hummer, D. G. 1994, MNRAS, 268, 109
Hummer, D. G., & Storey, P. J. 1998, MNRAS, 297, 1073
Fano, U., & Cooper, J. W. 1968, Reviews of Modern Physics, 40, 441
Ferland, G. J., Peterson, B. M., Horne, K., Welsh, W. F., & Nahar, S. N. 1992, ApJ, 387, 95
Ferland, G. J., Korista, K. T., Verner, D. A., et al. 1998, PASP, 110, 761
Ferland, G. J., Porter, R. L., van Hoof, P. A. M., et al. 2013, Rev. Mexicana Astron. Astrofis., 49, 137
Foster, A. R., Ji, L., Smith, R. K., & Brickhouse, N. S. 2012, ApJ, 756, 128
Gnat, O., & Ferland, G. J. 2012, ApJS, 199, 20
Gu, M. F. 2003, ApJ, 589, 1085
Kaastra, J. S., Mewe, R., & Nieuwenhuijzen, H. 1996, UV and X-ray Spectroscopy of Astrophysical and Laboratory Plasmas, 411
Kaastra, J. S., Bykov, A. M., Schindler, S., et al. 2008, Space Sci. Rev., 134, 1
Kallman, T. R., & McCray, R. 1982, ApJS, 50, 263
Kim, Y. S., & Pratt, R. H. 1983, Phys. Rev. A, 27, 2913
Kinkhabwala, A., Sako, M., Behar, E., et al. 2002, ApJ, 575, 732
LaMothe, J., & Ferland, G. J. 2001, PASP, 113, 165
Liedahl, D. A., & Paerels, F. 1996, ApJ, 468, L33
Lykins, M. L., Ferland, G. J., Porter, R. L., et al. 2013, MNRAS, 429, 3133
Mao, J., & Kaastra, J. 2016, A&A, 587, A84
Nahar, S. N. 1999, ApJS, 120, 131
Osterbrock, D. E. 1989, Research supported by the University of California, John Simon Guggenheim Memorial Foundation, University of Minnesota, et al. Mill Valley, CA, University Science Books, 1989, 422 p.,
Ozawa, M., Koyama, K., Yamaguchi, H., Masai, K., & Tamagawa, T. 2009, ApJ, 706, L71
Raymond, J. C., Cox, D. P., & Smith, B. W. 1976, ApJ, 204, 290
Schure, K. M., Kosenko, D., Kaastra, J. S., Keppens, R., & Vink, J. 2009, A&A, 508, 751
Seaton, M. J. 1959, MNRAS, 119, 81
Seaton, M. J., Zeippen, C. J., Tully, J. A., et al. 1992, Rev. Mexicana Astron. Astrofis., 23, 19
Smith, R. K., Brickhouse, N. S., Liedahl, D. A., & Raymond, J. C. 2001, ApJ, 556, L91
Storey, P. J., & Hummer, D. G. 1991, Computer Physics Communications, 66, 129
Sutherland, R. S., & Dopita, M. A. 1993, ApJS, 88, 253
Tucker, W. H., & Gould, R. J. 1966, ApJ, 144, 244
Verner, D. A., Yakovlev, D. G., Band, I. M., & Trzhaskovskaya, M. B. 1993, Atomic Data and Nuclear Data Tables, 55, 233
Verner, D. A., & Ferland, G. J. 1996, ApJS, 103, 467